Paper:
James, T., Murray, T., Selmes, N., Scharrer, K. & O'Leary, M. Buoyant flexure and basal crevassing in dynamic mass loss at Helheim Glacier. *Nature Geoscience, 7*(8), 593-596.

http://dx.doi.org/10.1038/ngeo2204

Buoyant flexure controls summer dynamic mass loss at Helheim Glacier, Greenland

Timothy D. James*, Tavi Murray, Nick Selmes, Kilian Scharrer and Martin O'Leary

Glaciology Group, Department of Geography, Swansea University, Singleton Park, Swansea, SA2 8PP, United Kingdom

Corresponding author T.D. James (t.d.james@swansea.ac.uk)

Iceberg calving accounts for a significant proportion of annual mass loss from tidewater-terminating glaciers[1, 2] and was likely a major factor in the rapid demise of paleo-ice sheets[3]. Recent forecasts of sea-level contributions from the main outlet glaciers of the Greenland Ice Sheet find the majority of mass-loss will be dynamic in origin over the next two centuries [4]. However, despite the use of increasingly realistic, physically-based approaches for representing the important calving component, current models remain a coarse approximation of real calving mechanisms. This is due largely to a lack of observational data of glacier geometry required for the development of 3D time-evolving models[5]. Here we present a high temporal and spatial resolution record of daily digital elevation models (DEMs) of the calving margin of Greenland's Helheim Glacier during the summers of 2010 and 2011 derived from stereo terrestrial photography. Our results show that during these summers large (>1 km^3) calving events driven by buoyant flexure dominated dynamic mass loss at Helheim. This calving mechanism, common at Helheim and likely elsewhere in Greenland, is clearly an important first-order control on the ice sheet's mass balance. However, recent models favour surface-driven crevasse propagation as the first-order control on calving and thus could be misrepresenting dynamic mass-loss from the ice sheet.

A widely adopted approach for representing calving in glacier and ice sheet models due to its ability to simulate a wide variety of calving behaviour is to define calving front location as the point where transverse surface crevasses propagate to the waterline[11]. Although a simplification, crevasse depth is widely considered to be a first-order control on calving rate and with terminus position is ultimately a function of ice velocity, strain rate, ice thickness and water depth. The crevasse-depth model has been extended to include the sensitivity of calving rate to a depth of water in surface crevasses[11, 12, 13] and also the propagation of basal crevasses[5]. These advances have enabled the modelling of individual calving events[13] as well as the development of models that use assumed realistic and fully dynamic marine boundary conditions for forecasting of sea-level contributions[4]. However, due in large part to a lack of quantitative observational data, the true mechanisms of calving are still largely unknown and thus the development of a universal calving law remains unsolved.

Our high temporal and spatial resolution time series of DEMs of the Helheim calving margin (Figure S1) using stereo, terrestrial time-lapse photography (see Methods Section, Terrestrial and ASTER Photogrammetry) gives a detailed account of the evolution of the glacier terminus here presented in 24 hour time-steps. In 2010, Helheim experienced four major calving events between 11 and 30 July with a cumulative areal loss of ~5.06 km^2 (~8.0 km^2 extrapolated to include the area outside the camera view) (Figure 1). At this time, we have not generated volume estimates of the calving events due to the high uncertainty and lack of data coverage in available bed data sets[14, 15].

The daily evolution of the calving front is shown in longitudinal profiles along the main flowline of the glacier (Figure 2). The most striking feature (Figure 2a) is the large surface depression some 20-30 m in depth running parallel to and about 1.5 km up-glacier from the 11 July calving front. This depression developed over the weeks preceding calving during a period of no major calving activity as evidenced from June and early July 2010 stereo ASTER imagery. Depressions like this have been reported previously in the literature and have been attributed to dynamic thinning associated with glacier retreat down a reverse bed slope[10, 16].

On the first day of the time series, the front advanced (~22 m) and lifted (~5 m) and the depression advected downstream at approximately the speed of ice flow (Figure 2a). The glacier then experienced three significant calving events in close succession resulting in the glacier front retreating to the lowest point of the depression. The first of these calving events was captured in high resolution 10 second time-lapse imagery, which shows the formation of a backward-rotating iceberg measuring >4 km across-glacier and 300 m in the direction of glacier flow (Movie S2). Over the next 14 days (Figure 2b) the terminus advanced daily without calving during which time the ice surface lifted at the calving front, slowly at first, accelerating vertically (from 0 to ~8 m day^{-1}) as the next calving event approached. Most noticeably towards the end of the time series, the surface again became depressed to a depth of ~20 m below the height of the calving front and about 400 m up glacier from the terminus. Note the images show that the depression was not the result of an expanding rift(s) but rather the downward flexure of the surface coupled with the lifting front; evidence that the front section down-glacier of the depression was under rotation. On the last day of the time series, the fourth calving event occurred with the front again retreating to the low point of the depression.

We applied feature tracking to the daily images prior to the 12 July 2010 calving event to show glacier displacement along the image-space vertical axis (y_i) as an approximation of actual vertical displacement of the glacier front (see Methods Section, Feature Tracking). The results show the vertical displacement in the longitudinal profiles occurred across the entire visible calving front (Figure 3). The lifting of the front and formation of the associated up-glacier depression are clearly discernible in the imagery days before the iceberg finally detaches. The profiles show that the rotation of the front section accelerated as the calving event neared and ultimately lead to ice failure and calving. Poor lighting prior to the 29 July 2010 calving event prohibited their use in feature tracking, however the same mechanism of calving (rotation of the calving section) was also visible in these images.

An 11 day time series of topographic data from 2011 (Figure 2c) shows a thinner calving front advanced beyond the location of the 2010 depression with no sign of similar lifting of the calving front or any associated depression. Together with the observed advection of the depression in 2010, this suggests it is unlikely that a bed feature was responsible for the upward displacement of the surface at this location in 2010. Feature tracking applied to the images leading up to the four major 2011 calving events reveals that the same rotation of the glacier's front section preceded calving suggesting that the same style of calving dominated 2011's summer dynamic mass loss (Figure S3-Figure S5).

To put these results in a longer-term context we took profiles from DEMs generated using the 11 year ASTER record (2001 – 2012) (see Methods Section, Terrestrial and ASTER Photogrammetry), which show that the paired frontal lift and surface depression are common at Helheim (Figure 4). These lifted front sections occur at a multitude of positions in the fjord rather than in the same location. The 18 July 2004 ASTER scene captured a clearly rotated front section with the normally vertical calving face clearly visible in the satellite image due to its high rotation angle as the next calving event neared (Figure S6).

Our observations suggest that dynamic thinning over a bed depression is not driving these large calving events given: (i) the paired lifting/depression of the front section; (ii) the occurrence at multiple locations in the fjord; and (iii) the clear rotation of the calving section in the feature-tracked images. Similarly, the imagery shows no evidence of longitudinal stretching and widening of surface crevasses until after the surface depressions have collapsed making this mechanism unlikely to be the first-order control on dynamic mass loss at Helheim as often assumed in models. Thus, we also question the significance of the role of water-filled crevasses on dynamic mass loss at Helheim at least during the summers of 2010 and 2011. Our observations suggest it is unlikely that these calving events are driven by surface processes. While dynamic thinning and surface crevasses no doubt play an important role in calving dynamics, we conclude that the dominant mechanism of dynamic mass loss at Helheim during the 2010 and 2011 summer season was flexure due to buoyancy-induced rotation.

There is considerable literature on buoyancy-induced rotation at marine and lacustrine termini (see ref. 17). Buoyancy forces result when the terminal surface is lowered relative to water height causing an otherwise grounded glacier to thin, becoming increasingly out of buoyant equilibrium. As buoyancy forces increase the ice must rotate to restore equilibrium either slowly by creep or rapidly by fracture propagation[17]. This mechanism is consistent with our observations and thus we consider potential causes of increasing buoyant flexure at Helheim's terminus.

In order for buoyancy to cause the events we have observed, the ice must be lowered relative to water height. Previous studies have reported that increasing buoyancy results when surface ablation causes ice to thin below flotation[18]. Recent models estimate an average summer ablation of ~0.055 m d^{-1} at Helheim's calving margin[19]. While this is small, buoyancy is believed to be insufficient for rotating large, full-glacier-thickness icebergs unless the calving portion of the glacier is near flotation[20]. Therefore, even small changes in surface elevation may be significant. However, we find that given the high flow speed of the glacier at the calving margin (>20 m d^{-1}), the daily evolution of the calving front observed between two backward-rotating calving events (Figure 2b) is consistent with the glacier being driven below flotation into deeper water at a rate faster than it can adjust. A similar phenomenon has been seen downstream of the grounding line of ice shelves (e.g. ref. 21). Figure 5 presents a schematic of our interpretation of the calving we have observed at Helheim. While the role of bottom crevasses is unknown, it has been suggested that they are likely to form in areas of high longitudinal strain rates and low basal effective pressure[22] as would be expected at Helheim's calving front.

The majority of calving events we observed at Helheim produced overturning icebergs. Atypically, the full width event on 12 Aug 2011 (Figure S5) produced an overturning iceberg on the south side of the fjord where the calving section width-to-height ratio (ε) was small and a tabular iceberg on the north side where ε was considerably larger. While frontal uplift was only seen on the south side, a depression was visible across the calving width though significantly less pronounced on the north side. The factors controlling ε here, shown to be key in determining the style of calving[20], are unknown but likely involve a complex interplay between the factors described in Figure 5 and in particular the effects of subglacial discharge and fjord circulation on subaqueous melting. This may be key in providing an link between calving behaviour and fjord temperatures/circulation[23] and an explanation of any seasonal variation in calving style and rate that is more consistent with observations than seasonal water in crevasses.

Understanding the mechanisms behind large calving events is vital for producing reliable models to forecast Greenland's future contribution to sea-level. Models typically reproduce observed glacier behaviour over relatively short time-scales which may be insufficient for extrapolation into the future if not based on the real physical processes. We provide improved observations of calving during two summers at Helheim Glacier providing a detailed characterisation of typical large calving events. Our results show that large, overturning icebergs begin rotating visibly several days before detachment from the glacier under buoyancy forces characterised by a paired lifting and depression of the calving section. Our results suggests that treatment of the calving criterion based on the penetration of air and water-filled surface crevasses to the waterline, which has previously been used as a first-order approximation of calving[11, 13], is missing key elements of calving dynamics and could misrepresent dynamic mass-loss from the ice sheet. However, factors controlling the style and rate of calving, especially bathymetry, fjord temperatures and circulation (and their effects on subaqueous melting) are unknown and it is likely that the primary control on calving changes over time. Our research highlights the many unknowns that persist about the drivers of calving and further work that needs to be undertaken.

Methods

Helheim Glacier is a major outlet of the Greenland Ice Sheet draining an area of ~52,000 km^2. Its recent behaviour has been under much scrutiny due to reports of acceleration[2, 24, 25], retreat[25, 26, 27] and thinning[25, 26] found to occur quasi-synchronously with other marine-terminating glaciers in the southeast[25, 28]. As the calving front is the closest major outlet glacier to southeast Greenland's main settlement, Tasiilaq, Helheim has been a primary target of data collection efforts over the last decade.

Terrestrial and ASTER Photogrammetry. In the summers of 2010 and 2011, we installed two 15.1 megapixel Canon 50D digital single-lens reflex (DSLR) cameras on the south shore of Helheim Fjord ~300 m apart and ~3.5 km down-fjord from the 2010 calving front (Figure 1). We used fixed 28 mm focal length lenses, which are sufficiently wide-angle to capture the majority of the glacier terminus without needing to be too far away thereby maximising image detail but with minimal distortion. Camera viewsheds and the area of image overlap enabling the extraction of elevation models are shown in Figure 1. The camera clocks were manually synchronised and set to take an image every 60 minutes, 24 hours a day. Clock drift was <15 seconds over a period of several months. In 2010, the cameras were powered with internal batteries, which provided hourly collection between 11 to 30 July (20 days, ~500 images). In 2011, 11 days of stereo imagery were collected from 27 June to 08 July due to a power failure in one camera but mono imagery was collected to 29 August.

Daily DEMs were generated using images taken at 0830 UTC due to optimal lighting of the calving front. Camera calibration was used to model and minimise focal length and lens distortion errors. Ground control points (GCPs), which link 2D image space to 3D ground space were extracted from stable areas of 2007 lidar DEMs following the methodology in ref. 29. DEMs were produced from stereo imagery using the 3D viewing capabilities of the

SOCET SET digital photogrammetry suite which is key for pinpointing the location of the GCP in the images. The photogrammetric bundle adjustment and DEM extraction was carried out in Topcon's ImageMaster.

DEMs were extracted nominally on a 5 m grid, where image resolution permitted since, with oblique imagery, image resolution decreases with distance from the cameras. These factors as well as the complicated surface topography meant the resulting topographic model took the form of an irregular cloud of xyz coordinate triplets with a maximum resolution of 5 m but that dropped with increasing distance from the camera. To simplify processing, the point clouds were interpolated to a regular 10 m grid using a local polynomial approach that assigns values on the grid using a weighted least squares fit to data within a user specified search window of 50 m. This window size was found to preserve sufficient surface detail for comparison while eliminating higher frequency elevation variations. An example of the resulting DEMs is given in Fig. S1.

The quality of DEMs of a dynamic surface like the calving margin of Helheim Glacier is difficult to quantify. For the terrestrial imagery, the photogrammetric block adjustment uses measured points and camera calibration information to predict the location and attitude of the cameras whose positions were surveyed with differential global positioning system data (DGPS) yielding an indication of the quality of the image block adjustment. The root mean square error (RMSE) of the predicted camera positions (Table S1) were sub-2m in XY and sub-metre in Z indicating a high relative accuracy between DEMs. Comparison to DGPS camera positions give the absolute accuracy of the DEMS. Typically, error due to the image correlation stage of DEM generation is evaluated by comparing the data to a ground truth data set, which is of course not available here. Therefore, we conservatively estimate the error of our DEMs at ±1 m in the vertical and ±5 m horizontal at the calving front (both degrading with distance from the cameras). We base these estimates on the block adjustment results and the ability of our DEMs to easily resolve the daily flow of the glacier which is expected to be ~20 m day^{-1}.

We produced DEMs from stereo ASTER imagery at 50 m resolution using the ASTER sensor model of BAE Systems Socet SET digital photogrammetry suite. While it is theoretically possible to produce ASTER DEMs at the same resolution as the imagery (15 m), the quality control of such a large and dense data set on such an irregular surface is difficult and unnecessary for characterising the important changes at Helheim. Similarly to the terrestrial photographs, ground control points were extracted from the 2007 lidar DEM. The processing of the imagery was carried out entirely in Socet Set where the software's 3D viewing capabilities enabled the accurate measurement of ground control points in the image plane. The average root mean square error (RMSE) of the photogrammetric block adjustment was 5.2 m in 5.2 m in Y and 1.1 m in Z suggesting a good fit of the sensor model to the image measurements. Due to low resolution of ASTER imagery (15 m) the quality of the resulting DEM will be lower than the RMSE of the model fit to image measurements. Quality will also be negatively affected by poor image contrast on dark and bright surfaces. We estimate plannimetric error to be ±8 m and elevation error in the ASTER DEMs to be ±2.5 m.

Feature Tracking. There is a large amount of spatial information recorded in photographic time series that becomes evident when manually 'flicking' through a data set. To provide a simple means of quantifying the evolution of the Helheim calving front as captured in our time series, we used the California Institute of Technology's COSI-Corr orthorectification and feature tracking module created for integration in the ENVI environment[30]. COSI-Corr was developed primarily for satellite and airborne images (i.e. near vertical or nadir viewing angle) and typically, images are orthorectified prior to image correlation to provide displacements in ground coordinates. The orthorectification of high oblique imagery (i.e. where the horizon is visible) is difficult and was unnecessary for demonstrating the movement of the ice at the calving front. COSI-Corr outputs the x and y components of displacement in image space (x_i, y_i). In this image configuration, ice displacement at the calving front due to glacier flow is dominantly along the x_i image axis. Therefore, we approximate vertical ice displacement using movement along the y_i axis. This assumption degrades towards the left side of the image where there is a larger component of glacier flow along the y_i axis, but the rotation of the front section remains clearly visible. Displacement measured on the stationary mountains suggests that the errors in these figures is ~1 pixel.

Acknowledgements

TDJ was supported by The Leverhulme Trust GLIMPSE Project (F/00391/J) and the Climate Consortium for Wales (C3W). NS and KS were also supported by The Leverhulme Trust. Field work was funded by The Leverhulme Trust, a Royal Geographical Society EPSRC Geographical Research Grant (20IGC 01/10), NERC (NE/I007148/1) and the European Union Seventh Framework Programme [FP7/2007-2013] under grant agreement n° 262693 [INTERACT]. ASTER imagery were acquired through NASA's Land Processes Distributed Active Archive Center (LP DAAC) with thanks to Operation IceBridge and Bill Krabill. The authors would also like to acknowledge software support from Nick Russill at TerraDat Geophysics (Image Master) and François Ayoub (COSI-corr). We acknowledge the use of bed DEM from CReSIS generated with support from NSF grant ANT-0424589 and NASA grant NNX10AT68G.

Author Contributions

TDJ developed the methodology, undertook the analysis and interpretation and wrote the manuscript. TM was the grant-holder and contributed to data collection and interpretation.

NS and KS contributed to methodological development and data collection. MO contributed to the interpretation. All authors contributed to the manuscript preparation.

References

1. Hagen J. O., Kohler J., Melvold K.& Winther J. G. Glaciers in Svalbard: mass balance, runoff and freshwater flux. *Polar Res.* **22**, 145-159 (2003).

2. Rignot E.& Kanagaratnam P. Changes in the velocity structure of the Greenland ice sheet. *Science* **311**, 986-990 (2006).

3. van der Veen C. J. Calving glaciers. *Prog. Phys. Geog.* **26**, 96-122 (2002).

4. Nick F. M., Vieli A., Andersen M. L., Joughin I., Payne A., Edwards T. L.*, et al.* Future sea-level rise from Greenland's main outlet glaciers in a warming climate. *Nature* **497**, 235-238 (2013).

5. Nick F. M., van der Veen C. J., Vieli A.& Benn D. I. A physically based calving model applied to marine outlet glaciers and implications for the glacier dynamics. *J. Glaciol.* **56**, 781-794 (2010).

6. Meier M. F.& Post A. Fast tidewater glaciers. *J. Geophys. Res.* **92**, 9051-9058 (1987).

7. Pfeffer W. T., Dyurgerov M., Kaplan M., Dwyer J., Sassolas C., Jennings A.*, et al.* Numerical modeling of Late Glacial Laurentide advance of ice across Hudson Strait: Insights into terrestrial and marine geology, mass balance, and calving flux. *Paleoceanography* **12**, 97-110 (1997).

8. van der Veen C. J. Tidewater calving. *J. Glaciol.* **42**, 375-385 (1996).

9. Vieli A., Funk M.& Blatter H. Flow dynamics of tidewater glaciers: a numerical modelling approach. *J. Glaciol.* **47**, 595-606 (2001).

10. Vieli A., Jania J.& Kolondra L. The retreat of a tidewater glacier: observations and model calculations on Hansbreen, Spitsbergen. *J. Glaciol.* **48**, 592-600 (2002).

11. Benn D. I., Hulton N. R. J.& Mottram R. H. 'Calving laws', 'sliding laws' and the stability of tidewater glaciers. *Ann. Glaciol.* **46**, 123-130 (2007).

12. Vieli A.& Nick F. M. Understanding and modelling rapid dynamic changes of tidewater outlet glaciers: issues and implications. *Surv. Geophys.* **32**, 437-458 (2011).

13. Cook S., Zwinger T., Rutt I. C., O'Neel S.& Murray T. Testing the effect of water in crevasses on a physically based calving model. *Ann. Glaciol.* **53**, 90-96 (2012).

14. Gogineni P. CReSIS Radar Depth Sounder Data, Lawrence, Kansas, USA. Digital Media. http://data.cresis.ku.edu/. 2012.

15. Bamber J. L., Griggs J. A., Hurkmans R. T. W. L., Dowdeswell J. A., Gogineni S. P., Howat I.*, et al.* A new bed elevation data set for Greenland. *The Cryosphere* **7**, 499-510 (2013).

16. Joughin I., Howat I., Alley R. B., Ekstrom G., Fahnestock M., Moon T.*, et al.* Ice-front variation and tidewater behavior on Helheim and Kangerdlugssuaq Glaciers, Greenland. *J. Geophys. Res.* **113**, F01004 (2008).

17. Benn D. I., Warren C. R.& Mottram R. H. Calving processes and the dynamics of calving glaciers. *Earth-Sci. Rev.* **82**, 143-179 (2007).

18. Howarth P. J.& Price R. J. The proglacial lake of Breiðamerkurjökull and Fjallsjökull, Iceland. *Geogr. J.* **135**, 573-581 (1969).

19. Andersen M. L., Larsen T. B., Nettles M., Elosegui P., van As D., Hamilton G. S.*, et al.* Spatial and temporal melt variability at Helheim Glacier, East Greenland, and its effect on ice dynamics. *J. Geophys. Res.-Earth* **115**, (2010).

20. Amundson J. M., Fahnestock M., Truffer M., Brown J., Luthi M. P.& Motyka R. J. Ice mélange dynamics and implications for terminus stability, Jakobshavn Isbrae Greenland. *J. Geophys. Res.-Earth* **115**, (2010).

21. Vaughan D. G. Tidal flexure at ice shelf margins. *J. Geophys. Res.* **100**, 6213-6224 (1995).

22. Van der Veen C. J. Fracture mechanics approach to penetration of bottom crevasses on glaciers. *Cold Reg. Sci. Technol.* **27**, 213-223 (1998).

23. O'Leary M.& Christoffersen P. Calving on tidewater glaciers amplified by submarine frontal melting. *The Cryosphere* **7**, 119-128 (2012).

24. Luckman A., Murray T., de Lange R.& Hanna E. Rapid and synchronous ice-dynamic changes in East Greenland. *Geophys. Res. Lett.* **33**, L03503, doi: 03510.01029/02005GL025428 (2006).

25. Howat I. M., Joughin I., Fahnestock M., Smith B. E.& Scambos T. A. Synchronous retreat and acceleration of southeast Greenland outlet glaciers 2000-06: ice dynamics and coupling to climate. *J. Glaciol.* **54**, 646-660 (2008).

26. Howat I. M., Joughin I.& Scambos T. A. Rapid changes in ice discharge from Greenland outlet glaciers. *Science* **315**, 1559-1561 (2007).

27. Moon T.& Joughin I. Changes in ice front position on Greenland's outlet glaciers from 1992 to 2007. *J. Geophys. Res.-Earth* **113**, (2008).

28. Murray T., Scharrer K., James T. D., Dye S. R., Hanna E., Booth A. D.*, et al.* Ocean regulation of glacier dynamics in south-east Greenland and implications for ice-sheet mass changes. *J. Geophys. Res.-Earth* **115**, doi: 10.1029/2009JF001522 (2010).

29. James T. D., Murray T., Barrand N. E.& Barr S. L. Extracting photogrammetric ground control from lidar DEMs for change detection. *Photogramm. Rec.* **21**, 310-326 (2006).

30. Ayoub F., Leprince S.& Avouac J. P. Co-registration and correlation of aerial photographs for ground deformation measurements. *ISPRS J. Photogramm.* **64**, 551-560 (2009).

Figures

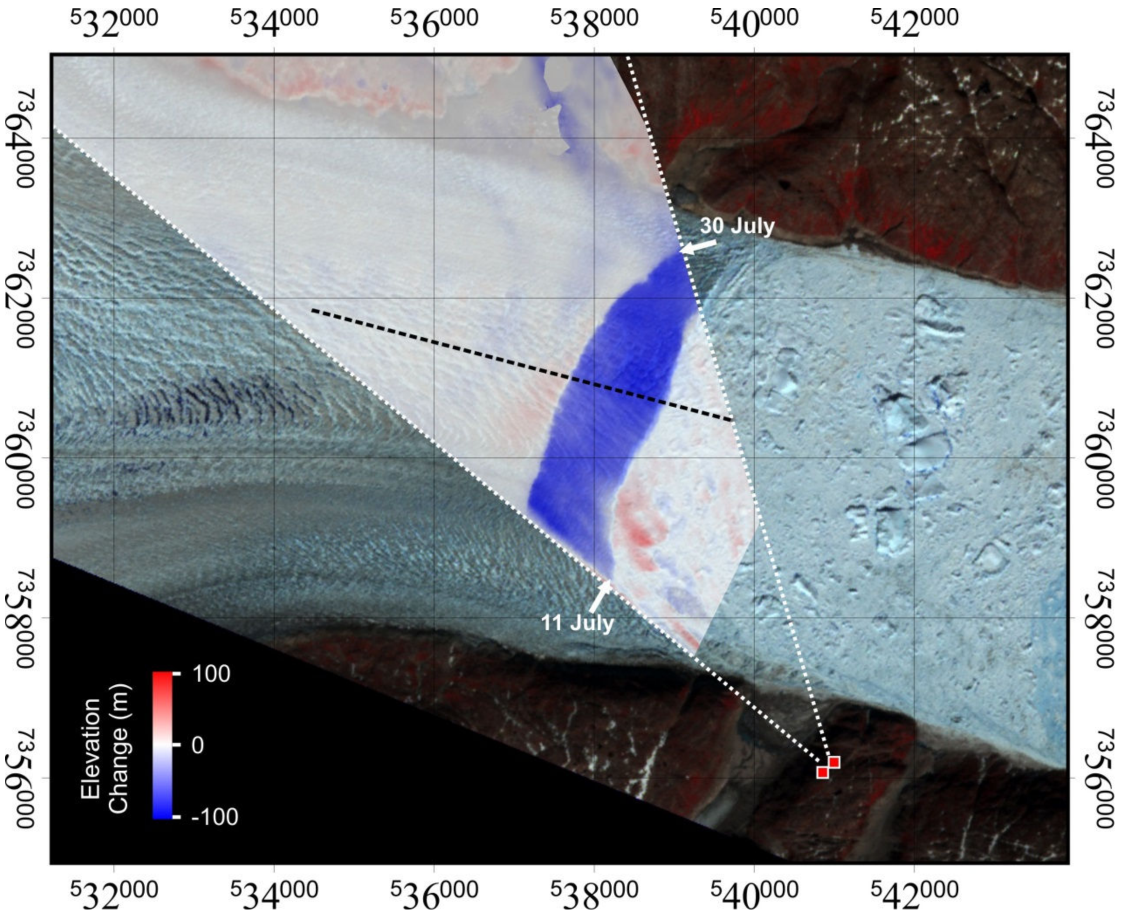

Figure 1 | Camera location with differenced DEM. Camera stations on the south side of Helheim Fjord are shown on this 08 July 2010 ASTER false colour composite orthoimage. Approximate stereo view-shed of the cameras is shown and the location of the profiles in Figure 2. Elevation changes at Helheim from 11 to 30 July, 2010 (front positions indicated) are overlaid showing ice loss of ~4.0 km^2 in the cameras' view-shed and ~0.29 km^3 above sea-level volume loss. Negative change anomaly in the top right of overlay are errors associated with a mountain shadow. Large elevation changes in the ice mélange show the movement of icebergs in the fjord and the production of new icebergs by the calving events.

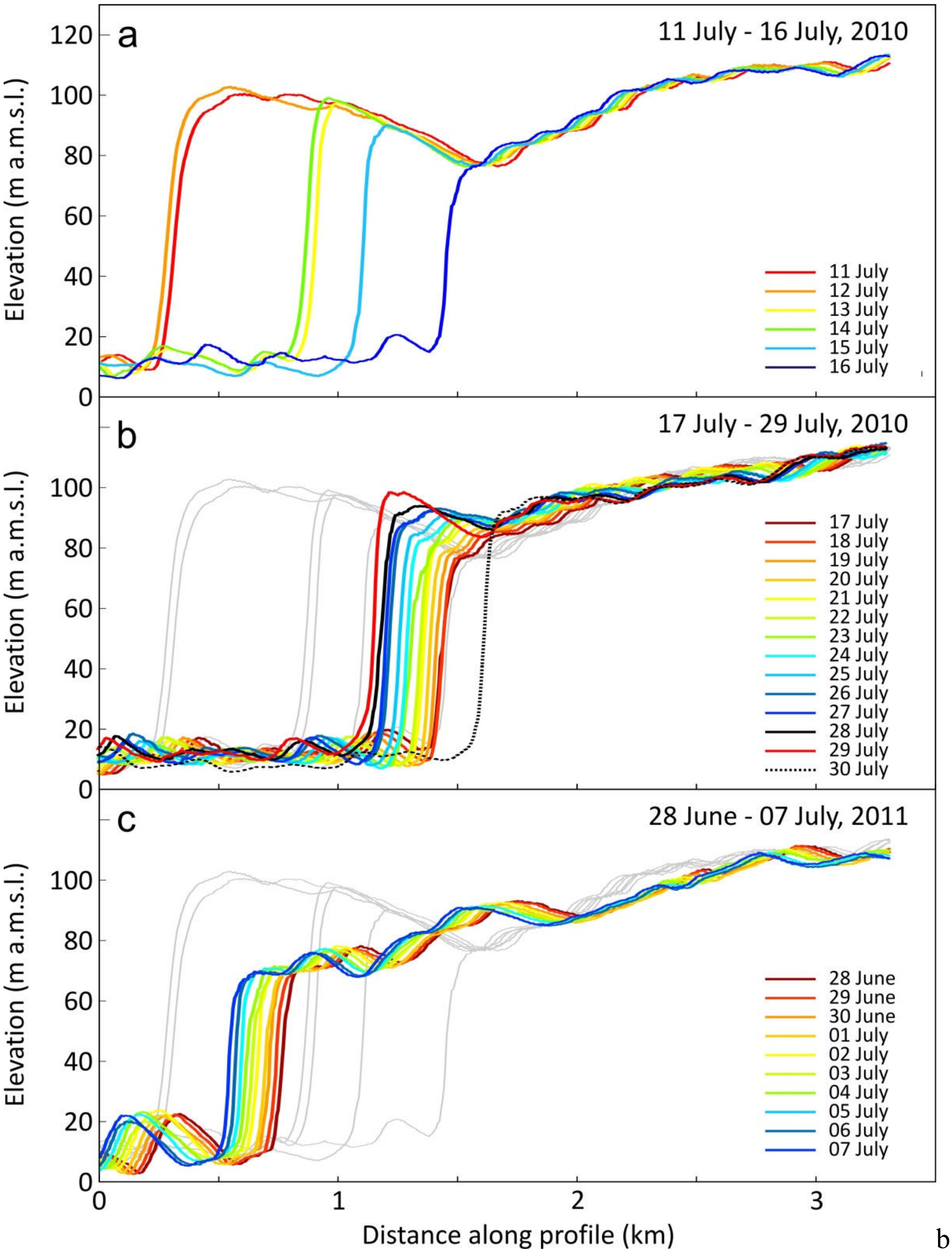

b

Figure 2 | Longitudinal elevation profiles on Helheim central flow line derived from stereo terrestrial photographs. Location of profiles is shown in Figure 1. (a) In the first six days of the time series the glacier terminus experienced three significant calving events causing the front to retreat to a pre-existing depression which the ASTER record shows had been deepening over the preceding period of minimal frontal activity. (b) With the profiles from (a) in the background, over the next 14 days, as the terminus advanced daily, the front lifted again forming a depression to which the front retreats on the last day of the time series. (c) In 2011, the front passes over the area of the 2010 depression without any sign of a similar surface low. As a guide, our error estimates for these profiles are about ± the line width. Elevations are above mean seal level (a.m.s.l.)

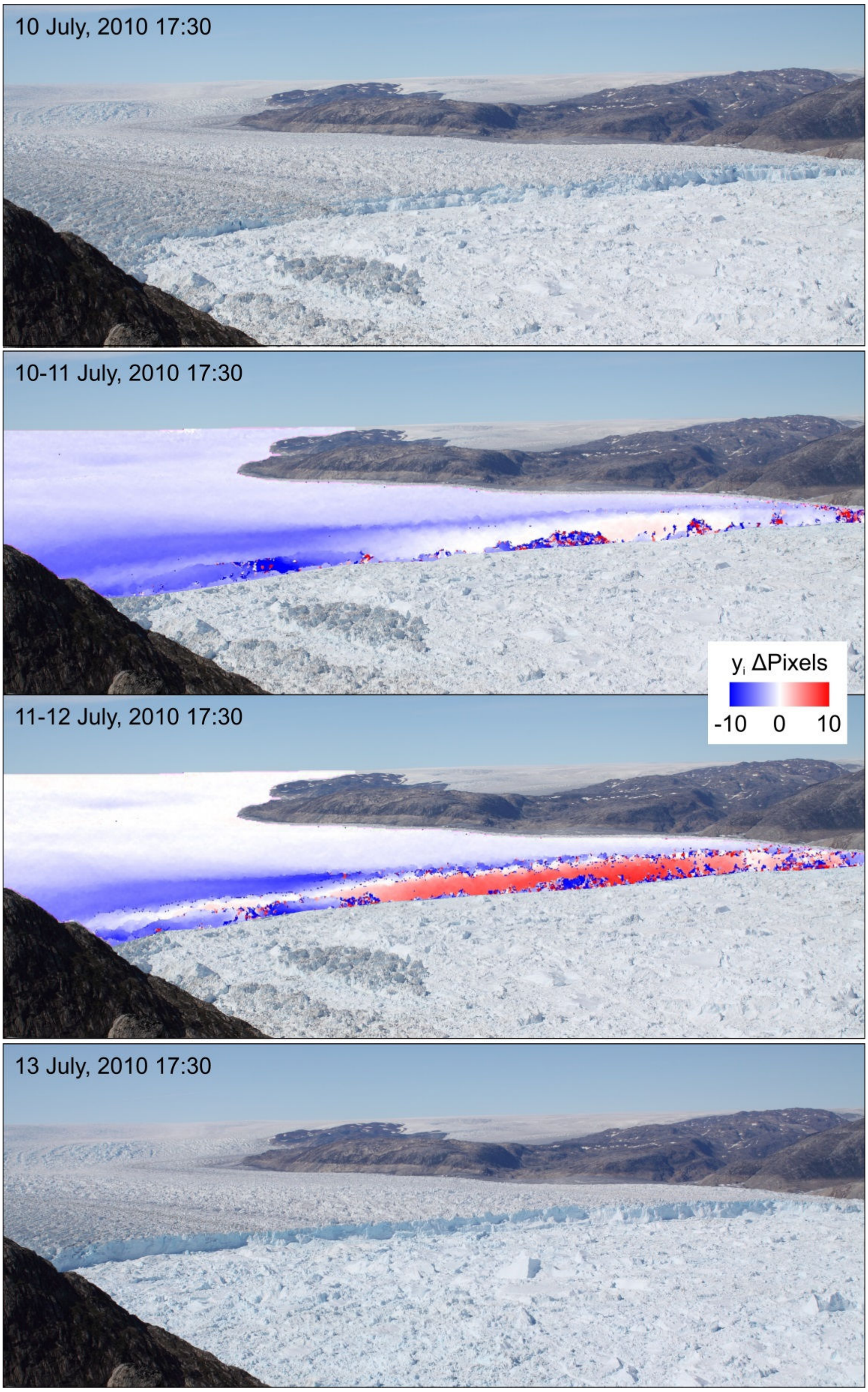

Figure 3 | Image feature tracking prior to the 12 July 2010 18:30 UTC calving event. This event was a full-width and full-depth calving event and was captured in 10 second time-lapse (see Movie S2). We applied feature tracking methods to the imagery over two 24 hour periods prior to the calving event to show displacement at the calving front. Displacement units are in pixels of displacement in image space (along y_i axis) with positive up, approximating vertical movement in real space.

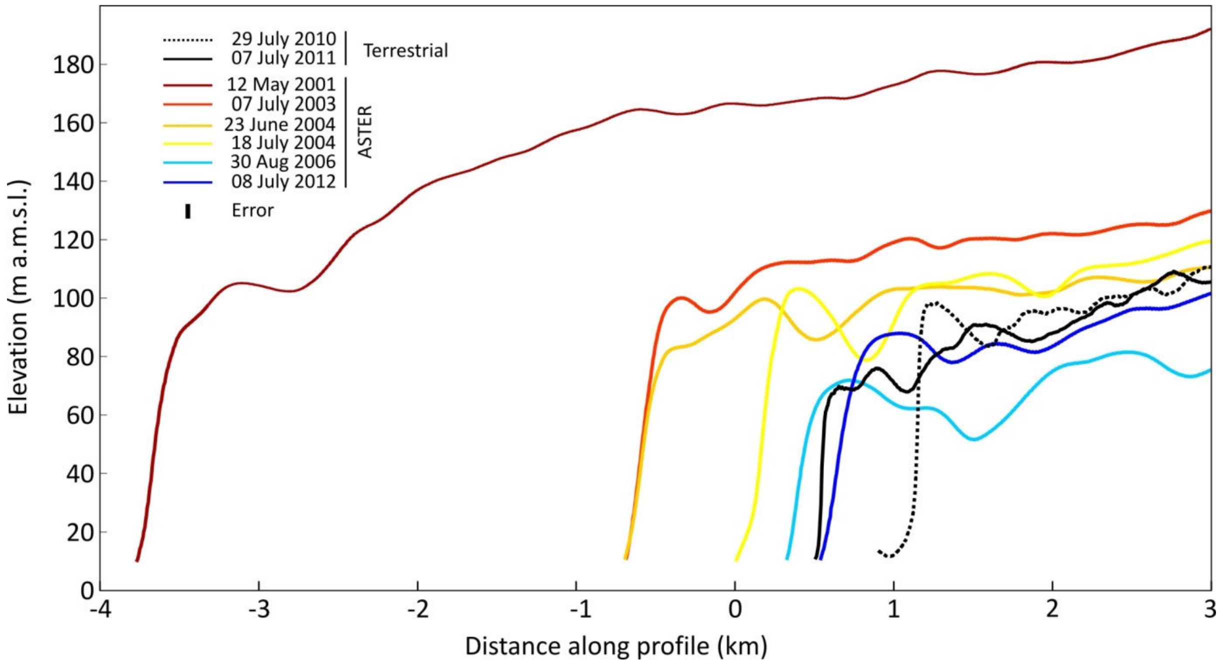

Figure 4 | 2010 and 2011 calving front in the context of 11 years of the ASTER record. Profiles derived from the terrestrial imagery for the beginning of both the 2010 and 2011 time series are shown.

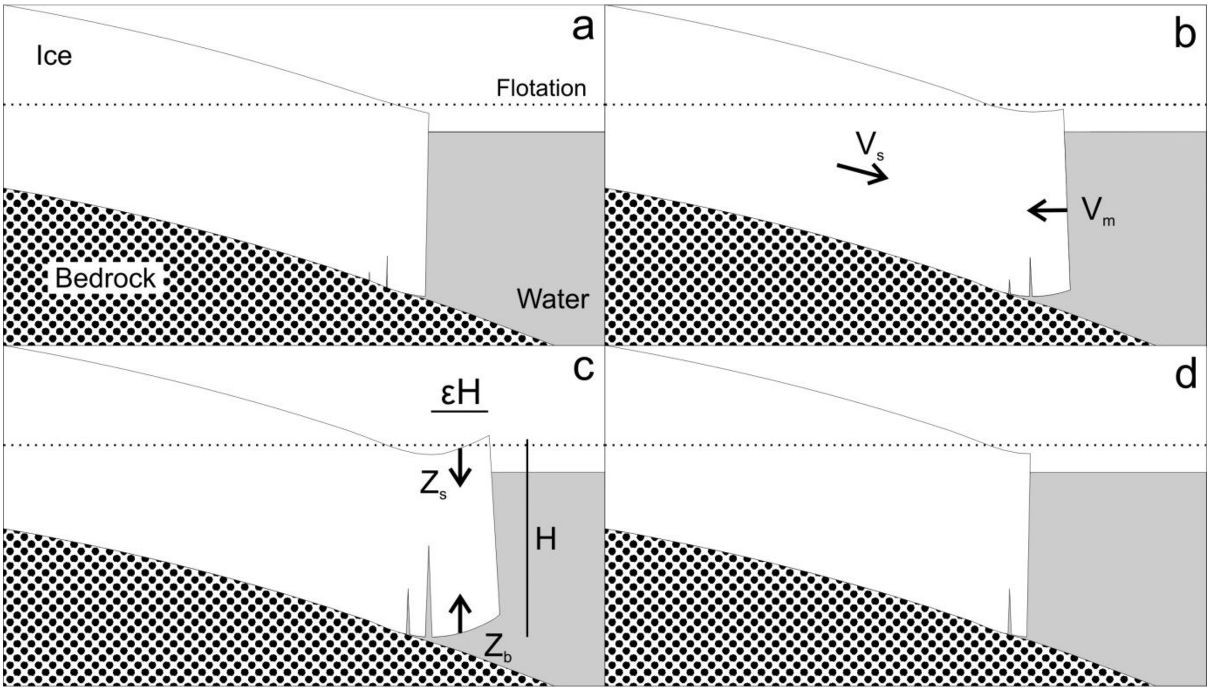

Figure 5 | Schematic of proposed calving by buoyant flexure. (a) The forward motion of the glacier drives the front section below flotation as it moves into deeper water. Note the likely presence of basal crevassing. (b) The ice initially responds to increasing buoyancy primarily by creep as indicated by the slow initial response of the calving front (17 – 28 July, Figure 2b). The bed slope, surface slope, ice velocity (V_s) and frontal subaqueous melting (V_m) will contribute to controlling the rate at which buoyancy increases. (c) In the days immediately prior to calving (28 – 29 July, Figure 2b) the rate of rotation increases dramatically, suggesting the propagation of a bottom crevasse(s), with rapid lifting of the front and depression of the surface at the hinge point of calving (likely at or near the grounding line). The dimensions of the calving section, εH and H, will in part be determined by a balance between surface (Z_s), basal (Z_b) and frontal subaqueous melting. (d) Finally, the buoyancy forces overcome the strength of the remaining intact ice and the ice eventually fails suddenly at the hinge point of the depression (29-30 July, Figure 2b).